PCCP

PAPER

View Article Online
View Journal | View Issue

Check for updates

Cite this: *Phys. Chem. Chem. Phys.*, 2020, **22**, 25146

Carbon dioxide and water incorporation mechanisms in $SrFeO_{3-\delta}$ phases: a computational study

L. J. Ford,[a] P. R. Slater,[b] J. K. Christie*[a] and P. Goddard*[c]

With a higher propensity for low temperature synthesis routes along with a move toward lower solid oxide fuel cell operating temperatures, water and carbon dioxide incorporation in strontium ferrite is of importance. Despite this, the mechanisms are not well understood. In this work, classical-potential-based computational techniques are used to determine the favourability of water and CO_2 incorporation mechanisms in both $SrFeO_{3-\delta}$ and $SrFeO_{2.5}$. Our studies suggest that intrinsic Frenkel and Schottky type defects are unlikely to form, but that water and carbon dioxide incorporation are favourable in both phases. Water incorporation is likely for both the cubic and brownmillerite phases, with hydroxyl ions preferring to sit on octahedral oxygen sites in both structures, causing slight tilting of the shared octahedra. Interstitial hydroxyl ions are only likely for the brownmillerite phase, where the hydroxyl ions are most stable between adjacent FeO_4 tetrahedral chains. Carbon dioxide incorporation *via* carbonate defects is most favourable when a carbonate molecule exists on an iron site, preferring the iron site with lower oxygen coordination. This involves formation of multiple oxygen vacancies surrounding the iron site, and thus we conclude that carbonate can trap oxygen vacancies.

Received 2nd July 2020,
Accepted 12th October 2020

DOI: 10.1039/d0cp03537h

rsc.li/pccp

Open Access Article. Published on 14 October 2020. Downloaded on 1/11/2026 11:58:37 AM.
This article is licensed under a Creative Commons Attribution-NonCommercial 3.0 Unported Licence.

1 Introduction

Solid oxide fuel cells (SOFCs) are likely to play an important role in the future of the world's sustainable energy system. Perovskite-based materials are among the most popular choice for SOFC electrode and electrolyte components as they often exhibit good conductive properties, stability and versatility. There are a large number of perovskite candidates,[1,2] one of which is $SrFeO_{3-\delta}$, which in its cubic phase exhibits high electronic and ionic conductivity and therefore has been identified as a promising cathode material.[3,4] At SOFC operating temperatures and with low oxygen content, strontium ferrite exists as brownmillerite-type $SrFeO_{2.5}$, which has lower conductivity than the cubic system due to oxygen vacancy ordering and therefore is currently less suitable for SOFC application. However, under doping, oxygen vacancy ordering can be lowered; other brownmillerite structures such as $Ba_2In_2O_5$[5] and $HSrCoO_{2.5}$[6] have shown promise regarding conductivity with oxyanion doping strategies for low- to intermediate-temperature SOFC applications.

At room temperature, strontium ferrite can exist in a number of different structures dependent on the oxygen content. The phases are cubic ($SrFeO_3$), tetragonal ($SrFeO_{2.875}$), orthorhombic ($SrFeO_{2.75}$) and brownmillerite-type ($SrFeO_{2.5}$). Cubic $SrFeO_3$ contains Fe^{4+} ions on the B site, each with an oxygen coordination of six, forming corner-sharing FeO_6 octahedra. In reality, pure $SrFeO_3$ is difficult to synthesise requiring high oxygen pressure. The brownmillerite-type $SrFeO_{2.5}$ structure contains only Fe^{3+} ions, and oxygen vacancy ordering results in alternate layers of Fe–O_6 octahedra and Fe–O_4 tetrahedra.[7] At temperatures above 850 °C, $SrFeO_{2.5}$ becomes cubic, but with a larger unit cell than the room temperature $SrFeO_3$ cubic perovskite.[8] The orthorhombic $SrFeO_{2.75}$ and tetragonal $SrFeO_{2.875}$ phases contain variable iron charges between 3+ and 4+. A recent DFT study on $SrFeO_{3-\delta}$ by Das *et al.* has elucidated the charge states of iron in these oxygen-vacancy-ordered phases, finding that the charge on Fe in square-pyramidal FeO_5 coordination remains 4+ and the charge on Fe in the FeO_6 octahedra varies between 4+ to 3+ due to the different d-orbital splitting of square-pyramidal and octahedral iron.[9]

To ensure high ionic conductivity in $SrFeO_{3-\delta}$, disordered oxygen vacancies must be present, avoiding the phase transition to a phase with ordered oxygen vacancies. Doping is a common strategy for inducing oxygen vacancies and modifying structure. Recent experimental work[3,4,10] has shown that oxyanion

[a] *Department of Materials, Loughborough University, Epinal Way, Loughborough, Leicestershire, LE11 3TU, UK. E-mail: J.K.Christie@lboro.ac.uk*
[b] *School of Chemistry, University of Birmingham, Edgbaston, Birmingham, B15 2TT, UK*
[c] *Department of Chemistry, Loughborough University, Epinal Way, Loughborough, Leicestershire, LE11 3TU, UK. E-mail: P.Goddard@lboro.ac.uk*

This journal is © the Owner Societies 2020

Open Access Article. Published on 14 October 2020. Downloaded on 1/11/2026 11:58:37 AM.
This article is licensed under a Creative Commons Attribution-NonCommercial 3.0 Unported Licence.

doping in perovskites can lead to favourable conductivity and structural effects. A study of Si incorporation into $SrFeO_{3-\delta}$ showed that Si^{4+} incorporation on the B site suppresses the formation of brownmillerite-type structures by forming SiO_4 tetrahedra which trap oxygen vacancies.[11] Interatomic-potential-based computational calculations allowed the structural and energetic details of the mechanisms in this work to be better understood.

In an operating fuel cell air electrode, both CO_2 and H_2O will likely be present, and it is useful therefore to look at their behaviour and mechanisms of their incorporation within SOFC component materials to discover their effect on structure and conductivity. McSloy *et al.* have used classical-potential-based computational methodology to look at carbon dioxide and water incorporation mechanisms and oxygen trapping in A_2BO_4 systems,[12,13] and found that carbonate defects are likely to be common impurities which trap oxygen ion defects. In some materials, water incorporation can lead to structural changes which alter the level of proton or oxygen–ion conduction. This increase in conductivity makes application for SOFCs more valuable both for use with an oxide ion or proton conducting electrolyte, and therefore water incorporation is worth investigating.

There are several reasons why looking at carbon dioxide incorporation is of interest in $SrFeO_3$. Carbon dioxide is present in air, and so consequently is present at the cathode of an SOFC and thus will inevitably interact with the cathode structure. In low- to intermediate-temperature SOFCs, carbonate may be thermally stable enough in the structure to consider incorporation likely, with potentially significant degradation or conductivity in the cathode material. In this paper, therefore, we present classical-potential-based computational work modelling H_2O and CO_2 incorporation into cubic $SrFeO_{3-\delta}$ and brownmillerite-type $SrFeO_{2.5}$ to look at the mechanisms of their inclusion using energy minimisation techniques.

2 Methodology

Interatomic-potential-based energy minimisation calculations were performed using the General Utility Lattice Program (GULP)[14,15] and structural images rendered using Visualisation for Electronic and STructural Analysis (VESTA).[16] Interatomic energies were based on the Born model for ionic solids where long- and short-range pairwise terms are used to describe the Coulombic, and the Pauli repulsive and van der Waals interactions, respectively. In this work, short-range ionic interactions were modelled using the Buckingham potential:[17]

$$\phi_{ij}(r) = A_{ij}\exp\left(\frac{r}{\rho_{ij}}\right) - \frac{C_{ij}}{r^6} \quad (1)$$

where ϕ_{ij} describes the potential energy resulting from the interaction of ions i and j separated by distance r. A_{ij}, ρ_{ij} and C_{ij} are empirically fitted potential parameters unique to the i–j ion pair.

Ionic polarisability is something which must also be accounted for in defective solid structure calculations: to model this we used the shell model developed by Dick and Overhauser,[18] which splits atoms into a separate charged core and shell connected by a spring force.

To find reliable potentials, existing Buckingham potential parameters from the literature[19–21] were used and tested on various strontium ferrite systems, and parameters were then fitted to the experimental structures of cubic $SrFeO_3$, tetragonal $SrFeO_{2.875}$, orthorhombic $SrFeO_{2.75}$ and brownmillerite like $SrFeO_{2.5}$, such that the potentials fitted were transferable to all structures. The Buckingham potential parameters used for the entirety of this work can be found in Table 1. The optimised structural geometries compared to experimental structures are shown in Table 2. The respective binary oxides SrO and Fe_2O_3

Table 1 Fitted interatomic potential parameters for all phases of strontium ferrite, listed in Table 2, and for CO_3^{2-} and OH^- molecules and interactions of these with strontium ferrite, based on values in the literature.[13,19–21,23–25] A short-range potential cutoff of 12 Å was enforced in all static lattice calculations

Interaction	A/eV	ρ/Å	C/eV Å^6
(a) Buckingham potentials			
Sr^{2+}–O^{2-}	1323.895825	0.34	0
Fe^{4+}–O^{2-}	1540	0.3249	0
Fe^{3+}–O^{2-}	1156.36	0.3249	0
O^{2-}–O^{2-}	22764.3	0.149	43
O^{2-}–H	311.97	0.25	0
O^{2-}–C	435.0	0.34	0
O_C–O_C	4030.3	0.2455	0
Interaction	**D/eV**	**β/Å^{-1}**	**r_0/Å**
(b) Morse potentials			
O_h–H	7.0525	2.1986	0.94850
O_C–C	5.0000	2.5155	1.20246
Interaction	**k_2/eV rad^{-2}**		**θ_0/°**
(c) Three body potential			
O_C–O_C–C	1.7887		120
Interaction	**k/eV**		**θ_0/°**
(d) Torsional term			
O_C–O_C–C–O_C	1.10		0.0
Species	**k_2/eV Å^2**		**k_4/eV Å^4**
(e) Spring interactions			
O_C	20.67		1000
O^{2-}	42		—
Sr^{2+}	21.53		—
Fe^{3+} and Fe^{4+}	304.7		—
Species	**Shell/e**		**Core/e**
(f) Shell model charges			
O^{2-}	−2.389		0.389
Sr	1.33		0.67
Fe^{3+}	−1.97		4.97
Fe^{4+}	−1.97		5.97
H	—		0.426
O_h	—		−1.426
C	—		1.45
O_C	0.23		−1.38

Open Access Article. Published on 14 October 2020. Downloaded on 1/11/2026 11:58:37 AM.
This article is licensed under a Creative Commons Attribution-NonCommercial 3.0 Unported Licence.

Table 2 Optimised structures generated using potentials compared with experimental data for cubic $SrFeO_3$, tetragonal $SrFeO_{2.875}$, orthorhombic $SrFeO_{2.75}$, brownmillerite-type $SrFeO_{2.5}$, layered iron oxycarbonate $Sr_4Fe_2O_6CO_3$ and strontium hydrogarnet $Sr_3Fe_2(OH)_{12}$

Parameter	Exptl[29]	Calc.	% Diff.
(a) $SrFeO_3$, space group $Pm\bar{3}m$ (221)			
a/Å	3.851	3.828	−0.60
$\alpha = \beta = \gamma$ (°)	90	90	
Parameter	Exptl[29]	Calc.	% Diff.
(b) $SrFeO_{2.875}$, space group $I4/mmm$ (139)			
a/Å	10.929	10.797	−1.21
c/Å	7.698	7.671	−0.34
$\alpha = \beta = \gamma$ (°)	90	90	
Parameter	Exptl[29]	Calc.	% Diff.
(c) $SrFeO_{2.75}$, space group $Cmmm$ (65)			
a/Å	10.974	10.895	−0.72
b/Å	7.702	7.688	−0.17
c/Å	5.473	5.446	−0.49
$\alpha = \beta = \gamma$ (°)	90	90	
Parameter	Exptl[30]	Calc.	% Diff.
(d) $SrFeO_{2.5}$, space group $Ima2$ (46)			
a/Å	15.598	14.851	−4.79
b/Å	5.661	5.628	−0.58
c/Å	5.531	5.491	−0.72
$\alpha = \beta = \gamma$ (°)	90	90	
Parameter	Exptl[26]	Calc.	% Diff.
(e) $Sr_4Fe_2O_6(CO_3)$, space group $I4/mmm$ (139)			
a/Å	3.878	3.831	−1.2
c/Å	27.982	27.846	−0.50
$\alpha = \beta = \gamma$ (°)	90	90	
Parameter	Exptl[27]	Calc.	% Diff.
(f) $Sr_3Fe_2(OH)_{12}$, space group $Ia3d$ (230)			
a/Å	13.202	13.443	3.16
$\alpha = \beta = \gamma$ (°)	90	90	

were also fitted to, in order to validate the potentials and ensure a good degree of transferability.

For intramolecular interactions between O–H and C–O in the water and carbon dioxide incorporation calculations respectively, interactions were described with a Morse potential[22] as it better describes the covalent character of the bond:

$$\phi_{ij}(r) = D_e[(1 - \exp(-a(1 - r_0)))^2 - 1] \quad (2)$$

where D_e and a are the depth and width of the potential well respectively and r_0 is the equilibrium bond distance.

For the carbon dioxide incorporation calculations, a three-body potential was used to energetically penalise deviation from the desired 120° of the carbonate group. This potential was of the form:

$$\phi_{ijk}(\theta_{ijk}) = \frac{1}{2}k_2(\theta_{ijk} - \theta_0)^2 \quad (3)$$

where θ_{ijk} is the bond angle between atoms i, j and k, and $\theta_0 = 120°$.

A torsional term was also included for the carbonate anion, to penalise it from deviating from the preferred flat configuration, this is of the form:

$$\phi_{ijkl}(\theta_{ijkl}) = k_4(1 - \cos(n\theta_{ijkl} - \theta_0)) \quad (4)$$

where i, j, k, l, θ, n, k_2 and k_4 represent the O–C–O–O particles in the CO_3^{2-} molecule, the torsional angle between labelled particles, number of stable minima, and the strength of the spring constants responsible for the magnitude of the energy penalty for deviation respectively.

The charges and potential parameter values for oxygen and hydrogen in molecular OH^- were taken from literature.[23] For the carbonate, potential parameters and charge values were also taken from literature.[13,24,25] These O–H and C–O potential parameters have also been successfully tested on $Sr_4Fe_2O_6CO_3$[26] and $Sr_3Fe_2(OH)_{12}$[27] structures to ensure transferability.

Point defects and single OH^- molecular defects were modelled using the Mott–Littleton method.[28] This method partitions the area encompassing the defect into two regions. Ions in the inner spherical region are relaxed explicitly, while those in the outer shell are handled by more approximate quasi-continuum methods.

Mott–Littleton region sizes were chosen to be 12 Å for the inner region and 24 Å for the outer region. Convergence tests showed no significant change (<0.1%) in defect energy for larger Mott–Littleton regions on OH^- defects.

For other, more complex, defects and defect cluster calculations the supercell method with a 6 × 6 × 6 cell for the cubic, 1 × 3 × 3 for the Brownmillerite and 4 × 4 × 4 for the $SrFeO_{2.7}$ phases was employed. The supercell sizes have been tested and are big enough so that the defects do not interact with their own equivalents in neighbouring cells of the bulk structure.

Classical potentials were chosen in favour of DFT methods for this work for several reasons. Firstly, there is sufficient existing experimental data and surrounding computational literature to fit and validate potentials which are transferable to the different phases of strontium ferrite. Secondly, the number of defect calculations required (particularly molecular defects) with the system size required would be computationally demanding using DFT methods. Finally, once a set of classical potentials are found, they can be used in future work to investigate molecular dynamics, which again would be computationally demanding *via* DFT methods.

Despite DFT calculations not being performed in this work, results from DFT calculations in the literature,[9] specifically, the computation of the oxygen vacancy formation energy, are considered due to the limitations of interatomic-potential methods to establish that energy accurately.

3 Results & discussion

3.1 Structural modelling

$SrFeO_{3-\delta}$ can adopt four different phases at room temperature dependent on the level of oxygen deficiency, with the ideal level

This journal is © the Owner Societies 2020

Open Access Article. Published on 14 October 2020. Downloaded on 1/11/2026 11:58:37 AM.
This article is licensed under a Creative Commons Attribution-NonCommercial 3.0 Unported Licence.

being for each δ = 0, 0.125, 0.25 and 0.5 giving iron oxidation states between Fe^{3+} and Fe^{4+}. These phases are shown in Fig. 3, and their space groups specified in Table 2. In the cubic phase, all iron atoms are octahedral and have a charge of 4+. In the tetragonal and orthorhombic phases, octahedral iron atoms are modelled with a charge of 4+, but the square planar iron atoms are modelled with a charge of 3+. Finally in the brownmillerite phase, all octahedra and tetrahedra were modelled with Fe^{3+} ions. It is important to acknowledge these as the Buckingham potentials in the model are different for Fe^{3+} and Fe^{4+}, as displayed in Table 1.

The DFT work on $SrFeO_{3-\delta}$[9] uses electronic relaxation and both pure structures and oxygen vacant structures do not show presence of Fe(3+) ions or O(1−) ions in the structure, so for the purposes of our work, these were not deemed necessary to look into explicitly. However, where necessary, iron charge compensation has been included in defect calculations using charge smearing, rather than a whole charge model. The smearing approach is supported by the DFT conclusion[9] that a whole charge model isn't likely to be accurate.

This work studies incorporation of OH^- and CO_3^{2-} in only the cubic and brownmillerite phases due to their relevance to fuel cells, however to ensure transferability in the interatomic potential model, the tetragonal and orthorhombic structures which both contain Fe^{3+} and Fe^{4+} ions were optimised using the potentials listed in Table 1 and compared to their experimental structures as well as for the cubic and brownmillerite-type structures, and the Ruddlesden–Popper phase $Sr_4Fe_2O_6CO_3$ and the hydrogarnet $Sr_3Fe_2(OH)_{12}$, as shown in Fig. 2. The calculated lattice parameters of all structures shows reasonable agreement with experimental data, as can be seen in Table 2, implying the potential is valid and transferable across all structures and phases, which is not trivial.

3.2 Intrinsic defects

3.2.1 Cubic $SrFeO_3$. For cubic $SrFeO_3$, all of the oxygen atoms are equivalent due to the cubic symmetry of the structure and the single Fe^{4+} oxidation state. All of the oxygen atoms are situated at the corners of symmetric Fe–O_6 octahedra, as shown in Fig. 1(a).

Our results, given in Table 3, show that all possible Frenkel and Schottky defects are unlikely to form spontaneously due to the high formation energies. However, it is important to note that in reality it is well known that oxygen vacancies do form in cubic $SrFeO_3$, with existing literature using DFT methods[9] finding the oxygen vacancy formation energy in pure $SrFeO_3$ to be very low, at 0.71 eV. In the work of this paper, the oxygen Frenkel energy is calculated to be 11.1 eV (5.55 eV per defect), which is considerably higher. This is because the real mechanism through which oxygen vacancies form is not of Frenkel-type as shown in Table 3. The real mechanism of oxygen vacancy formation instead involves a neutral $\frac{1}{2}O_2$ molecule being formed by the reaction: $O_O^{\times} \rightleftharpoons V_O^{\bullet\bullet} + \frac{1}{2}O_{2(g)} + 2e^-$ and the two remaining electrons reduce surrounding Fe^{4+}.

3.2.2 Brownmillerite $SrFeO_{2.5}$. For brownmillerite $SrFeO_{2.5}$, the same computational process was followed as for the cubic system, but there are three unique oxygen sites. The possible oxygen sites are corner-sharing between (1) a Fe–O_4 tetrahedron and a Fe–O_6 octahedron, (2) two octahedra, and (3) two

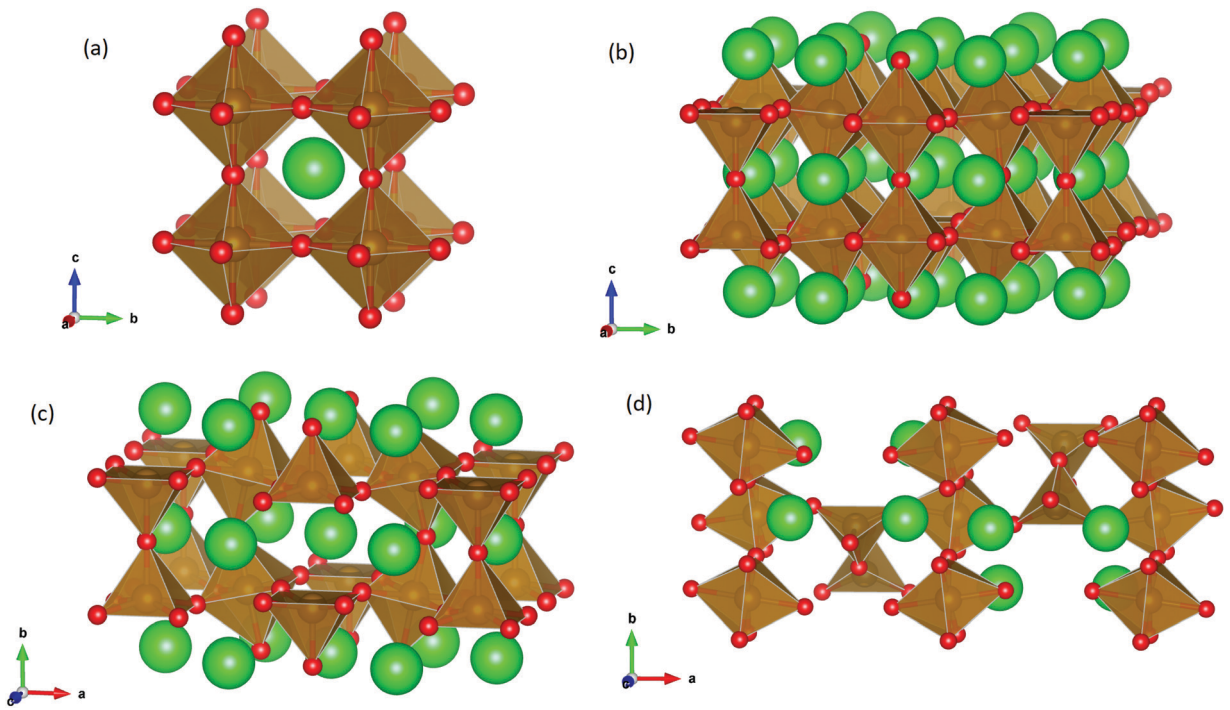

Fig. 1 Optimised structures of (a) cubic $SrFeO_3$, (b) tetragonal $SrFeO_{2.875}$, (c) orthorhombic $SrFeO_{2.75}$ and (d) brownmillerite $SrFeO_{2.5}$, with Sr, Fe and O ions represented as green, brown and red spheres respectively.

Open Access Article. Published on 14 October 2020. Downloaded on 1/11/2026 11:58:37 AM.
This article is licensed under a Creative Commons Attribution-NonCommercial 3.0 Unported Licence.

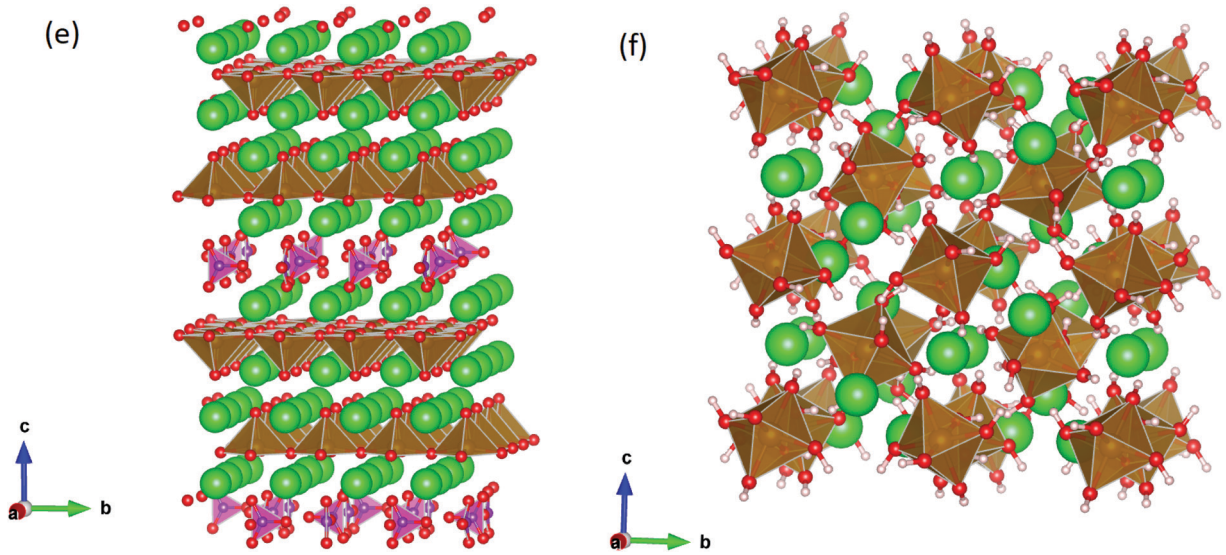

Fig. 2 Optimised structures of (e) the Ruddlesden–Popper-type iron oxycarbonate $Sr_4Fe_3O_6CO_3$ and (f) the strontium hydrogarnet $Sr_3Fe_2(OH)_{12}$, with H and C ions represented by white and purple spheres respectively.

Table 3 Intrinsic defect formation energies for cubic $SrFeO_3$, including Schottky and Frenkel defects. Schottky defect energies were calculated using simulated lattice energies of the binary oxides using the same potentials as in Table 1

Defect	KV equation	Energy (eV)/defect
O Frenkel	$O_O^{\times} \rightarrow V_O^{\bullet\bullet} + O_i^{''}$	5.6
Sr Frenkel	$Sr_{Sr}^{\times} \rightarrow V_{Sr}^{''} + Sr_i^{\bullet\bullet}$	7.3
Fe Frenkel	$Fe_{Fe}^{\times} \rightarrow V_{Fe}^{''''} + Fe_i^{\bullet\bullet\bullet\bullet}$	13.7
$SrFeO_3$ full Schottky	$Sr_{Sr}^{\times} + Fe_{Fe}^{\times} + 3O_O^{\times} \rightarrow V_{Sr}^{''} + V_{Fe}^{''''} + 3V_O^{\bullet\bullet} + SrFeO_3$	4.8
SrO partial Schottky	$O_O^{\times} + Sr_{Sr}^{\times} \rightarrow V_O^{\bullet\bullet} + V_{Sr}^{''} + SrO$	4.2

tetrahedra. There are therefore also two unique iron sites, one in the centre of an Fe–O_4 tetrahedron and the other in the centre of an Fe–O_6 octahedron; both are Fe^{3+}.

Table 4 shows that the most likely Frenkel defect is oxygen, with a formation energy of 3.57 eV. This Frenkel involves a vacancy of the oxygen site, corner-sharing between two octahedra. The other intrinsic Frenkel- and Schottky-type defects shown in Table 4 seem unlikely to form spontaneously. These findings are consistent with previous computational classical-potential work[31] on $SrFeO_{2.5}$, which found intrinsic defect energies for the brownmillerite system which are within 1 eV of our findings, despite using different potential parameters.

3.3 Water Incorporation

3.3.1 Cubic $SrFeO_3$. The mechanisms of water incorporation can include different reaction types, some involving the formation of interstitial OH^- ions and some involving the formation of hydroxide ions on an oxygen site. A number of simulations were carried out for hydroxide ions, both interstitial and on an oxygen site, in the cubic $SrFeO_3$ structure, to find out which geometrical arrangements are most energetically favourable. Plausible water incorporation mechanisms are written below in K–V notation as:

$$1.\ H_2O + 2O_O^{\times} \rightarrow 2OH_O^{\bullet} + O_i^{''}$$

Table 4 Intrinsic defect formation energies for brownmillerite-type $SrFeO_{2.5}$, including Schottky and Frenkel defects. Schottky defect energies were calculated using simulated lattice energies of the binary oxides using the same potentials as in Table 1

Defect	KV equation	Energy (eV)/defect
O Frenkel	$O_O^{\times} \rightarrow V_O^{\bullet\bullet} + O_i^{''}$	1.8
Sr Frenkel	$Sr_{Sr}^{\times} \rightarrow V_{Sr}^{''} + Sr_i^{\bullet\bullet}$	4.8
$SrFeO_{2.5}$ full Schottky	$Sr_{Sr}^{\times} + Fe_{Fe}^{\times} + \frac{5}{2}O_O^{\times} \rightarrow V_{Fe}^{'''} + V_{Sr}^{''} + \frac{5}{2}V_O^{\bullet\bullet} + \frac{1}{2}Sr_2Fe_2O_5$	3.3
SrO partial Schottky	$O_O^{\times} + Sr_{Sr}^{\times} \rightarrow V_O^{\bullet\bullet} + V_{Sr}^{''} + SrO$	3.2
Fe_2O_3 partial Schottky	$Fe_{Fe}^{\times} + \frac{3}{2}O_O^{\times} \rightarrow \frac{3}{2}V_O^{\bullet\bullet} + V_{Fe}^{'''} + \frac{1}{2}Fe_2O_3$	4.2

This journal is © the Owner Societies 2020

Open Access Article. Published on 14 October 2020. Downloaded on 1/11/2026 11:58:37 AM.
This article is licensed under a Creative Commons Attribution-NonCommercial 3.0 Unported Licence.

Table 5 $SrFeO_3$ water incorporation energies for mechanisms enumerated above. The table shows the constituent parts of the sum for each mechanism

Energy equation	Total formation energy (eV)
1. $E_{H_2O} = 2OH_O^{\bullet} + O_i'' + E_{PT} + E_{Morse}$	12.80
2. $E_{H_2O} = OH_O^{\bullet} + OH_i' + E_{PT} + E_{Morse}$	8.49
3. $E_{H_2O} = 2OH_O^{\bullet} - V_O^{\bullet\bullet} + E_{PT} + E_{Morse}$	1.70
4. $E_{H_2O} = 2OH_i' - O_i'' + E_{PT} + E_{Morse}$	4.19

$$2.\ H_2O + O_O^{\times} \rightarrow OH_O^{\bullet} + OH_i'$$

$$3.\ H_2O + V_O^{\bullet\bullet} + O_O^{\times} \rightarrow 2OH_O^{\bullet}$$

$$4.\ H_2O + O_i'' \rightarrow 2OH_i'$$

A series of calculations were performed using the Mott–Littleton method to find the most energetically favourable positions for $OH_O^{\bullet}$ and OH_i' defects.

Water incorporation energies (E_{H_2O}) and their energy equations are listed in Table 5. The E_{PT} term describes the proton transfer energy[32] of −9.74 eV in the reaction $H_2O + O^{2-} \rightarrow 2OH^-$. There is also a term, E_{Morse}, which accounts for the Morse potential energy released when a water molecule is broken, which is equal to twice the D parameter in the Morse potential between O_h and H.

These calculations suggest that mechanisms 1, 2 and 4 are unfavourable, which includes both mechanisms with an OH_i' defect as shown in Fig. 3. The most likely mechanism to occur is mechanism 3, with an energy of 1.7 eV, involving a hydroxide ion on an oxygen site $(OH_O^{\bullet})$ causing slight octahedral tilting, as shown in Fig. 4. This mechanism however requires a pre-existing oxygen vacancy: hence the oxygen-deficient cubic $SrFeO_{2.7}$ was also simulated. Experimentally it is well known that pure stoichiometric $SrFeO_3$ is difficult to synthesise due to the natural formation of oxygen vacancies.[33] Also, as discussed in Section 3.2.1, results from DFT simulations calculate the oxygen vacancy formation energy to be 0.71 eV. Therefore, it is reasonable to expect that oxygen vacancies will already be present in cubic $SrFeO_3$ and thus the conditions for water incorporation mechanism 3 to occur are likely.

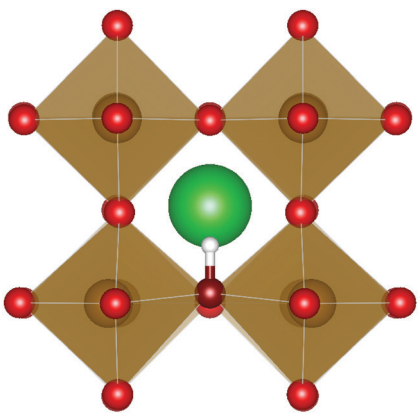

Fig. 3 The lowest energy hydroxide ionic defect on an oxygen site in cubic $SrFeO_3$. The hydrogen and hydroxide oxygen are shown by white and dark red spheres respectively.

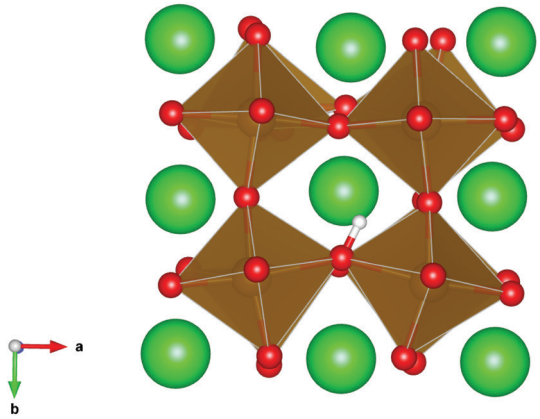

Fig. 4 The lowest energy hydroxide ionic defect on an oxygen site in cubic $SrFeO_{2.7}$, with oxygen vacancies present.

A number of clustering calculations were also performed using the supercell method with a 6 × 6 × 6 cell for two nearby hydroxide molecules on oxygen sites. Results from this suggest that it is slightly more favourable for two $OH_O^{\bullet}$ defects to cluster. The most favourable configuration for two hydroxide ions is on two nearest-neighbour oxygen sites where the two hydroxide ions are parallel to one another. The energy of incorporation per water molecule in this case is 1.53 eV, which is 0.17 eV lower than for two infinitely separated hydroxide ions. However, note that this is *via* mechanism 3 which requires the presence of an oxygen vacancy, thus for clustered hydroxide ions to be on neighbouring sites *via* water incorporation mechanism 3, two adjacent oxygen vacancies must be present. Clustering calculations for oxygen vacancies suggest that nearby oxygen vacancies repel one another; the difference in energy between two infinitely separated oxygen vacancies and two closest neighbouring ones is 1.32 eV (in favour of being infinitely separated). After considering this, we conclude that despite hydroxide molecules slight preference to cluster, the requirement of closest-neighbour oxygen vacancies makes this unlikely.

3.3.2 Brownmillerite $SrFeO_{2.5}$. Brownmillerite-type $SrFeO_{2.5}$ has ordered oxygen vacancies which reduce its ionic conductivity, but it is possible that water incorporation could increase the disorder of the oxygen vacancies and improve ionic conductivity and potentially protonic conductivity, making it more suitable for SOFC applications, particularly in conjunction with proton-conducting electrolytes.

The water incorporation mechanisms for the brownmillerite-type system are the same as those enumerated for the cubic system. Water incorporation energies and equations are listed in Table 6.

Similar to the cubic system, a series of calculations were performed using the Mott-Littleton method to find the most favourable positions for $OH_O^{\bullet}$ and OH_i'. These simulations

Open Access Article. Published on 14 October 2020. Downloaded on 1/11/2026 11:58:37 AM.
This article is licensed under a Creative Commons Attribution-NonCommercial 3.0 Unported Licence.

Table 6 Brownmillerite-type $SrFeO_{2.5}$ water incorporation energies for mechanisms enumerated above

Energy equation	Total formation energy (eV)
1. $E_{H_2O} = 2OH_O^{\bullet} + O_i'' + E_{PT} + E_{Morse}$	4.32
2. $E_{H_2O} = OH_O^{\bullet} + OH_i' + E_{PT} + E_{Morse}$	2.65
3. $E_{H_2O} = 2OH_O^{\bullet} - V_O^{\bullet\bullet} + E_{PT} + E_{Morse}$	0.75
4. $E_{H_2O} = 2OH_i' - O_i'' + E_{PT} + E_{Morse}$	0.98

suggest that mechanism 1 is most unlikely, followed by mechanism 2. Mechanism 3 and 4 have energies of under 1 eV and thus would be most likely to occur naturally in $SrFeO_{2.5}$ exposed to water. Fig. 5 shows the geometry of the most favourable $OH_O^{\bullet}$ and OH_i' defects respectively. For mechanism 3 which involves $OH_O^{\bullet}$ defects, the structural effect is slight deformation of the regular polyhedral geometry. For mechanism 4 which involves OH_i' defects, the structural impact is more significant as the hydroxide molecule bridges the gap between disconnected tetrahedral chains. This type of defect could have significant implications for oxide ion conductivity and could be a subject of future study.

Both of the more favourable incorporation mechanisms 3 and 4 involve an assumed impurity in the structure: mechanism 3 assumes an oxygen vacancy within the structure before water incorporation and mechanism 4 requires an oxygen interstitial. Given that the oxygen Frenkel energy is 1.8 eV per defect, it seems plausible to expect that the system would already contain a small amount of oxygen vacancies and interstitials. This, coupled with the energy in mechanism 2 of 2.65 eV suggests that water incorporation is viable in brownmillerite-type $SrFeO_{2.5}$, through mechanisms 2, 3 and 4.

Clustering simulations of brownmillerite-type strontium ferrite yielded similar results as the cubic case. OH^- defect pairs on neighbouring oxygen sites in all unique configurations do not differ significantly in energy from OH^- defects which are far apart from each other.

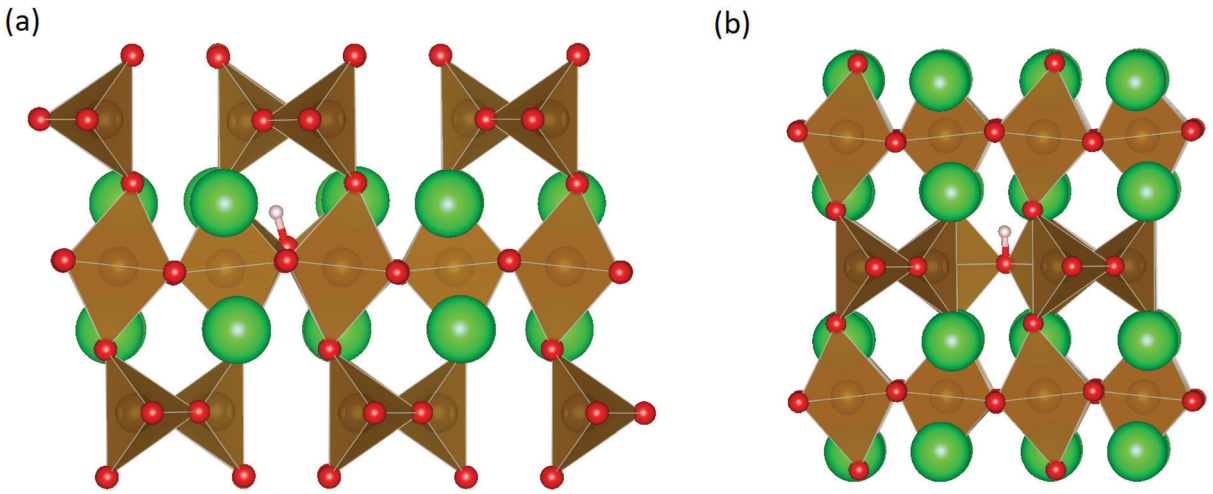

Fig. 5 The lowest energy $OH_O^{\bullet}$ (a) and OH_i' (b) in brownmillerite-type $SrFeO_{2.5}$. Sr, Fe, O and H ions are represented by green, brown, red and white spheres respectively. Both the Fe–O_6 octahedra and Fe–O_4 tetrahedra are represented in brown.

Table 7 Carbon dioxide incorporation energies for a 6 × 6 × 6 cubic $SrFeO_3$ supercell

Mechanism	Formation energy/defect (eV)
1(a) – $Fe_{Fe}^{\times} + O_O^{\times} + CO_2^{(g)} \rightarrow \left[(CO_3)_{Fe}'''''' + V_O^{\bullet\bullet}\right] + \frac{3}{2}V_O^{\bullet\bullet} + \frac{1}{2}(Fe_2O_3)$	2.72
1(b) – $Fe_{Fe}^{\times} + 2O_O^{\times} + CO_2^{(g)} \rightarrow \left[(CO_3)_{Fe}'''''' + 2V_O^{\bullet\bullet}\right] + \frac{1}{2}V_O^{\bullet\bullet} + \frac{1}{2}(Fe_2O_3)$	−0.6
1(c) – $Fe_{Fe}^{\times} + 3O_O^{\times} + CO_2^{(g)} \rightarrow \left[(CO_3)_{Fe}'''''' + 3V_O^{\bullet\bullet}\right] + \frac{1}{2}O_i'' + \frac{1}{2}(Fe_2O_3)$	−1.86
1(d) – $Fe_{Fe}^{\times} + 4O_O^{\times} + CO_2^{(g)} \rightarrow \left[(CO_3)_{Fe}'''''' + 4V_O^{\bullet\bullet}\right] + \frac{3}{2}O_i'' + \frac{1}{2}(Fe_2O_3)$	−1.93
1(e) – $Fe_{Fe}^{\times} + 5O_O^{\times} + CO_2^{(g)} \rightarrow \left[(CO_3)_{Fe}'''''' + 5V_O^{\bullet\bullet}\right] + \frac{5}{2}O_i'' + \frac{1}{2}(Fe_2O_3)$	−1.59
1(f) – $Fe_{Fe}^{\times} + 6O_O^{\times} + CO_2^{(g)} \rightarrow \left[(CO_3)_{Fe}'''''' + 6V_O^{\bullet\bullet}\right] + \frac{7}{2}O_i'' + \frac{1}{2}(Fe_2O_3)$	−1.84
2(a) – $O_O^{\times} + CO_2^{(g)} \rightarrow (CO_3)_O^{\times}$	3.81
2(b) – $2O_O^{\times} + CO_2^{(g)} \rightarrow \left[(CO_3)_O^{\times} + V_O^{\bullet\bullet}\right] + O_i''$	1.02
2(c) – $3O_O^{\times} + CO_2^{(g)} \rightarrow \left[(CO_3)_O^{\times} + 2V_O^{\bullet\bullet}\right] + 2O_i''$	1.10

 This journal is © the Owner Societies 2020

Open Access Article. Published on 14 October 2020. Downloaded on 1/11/2026 11:58:37 AM.
This article is licensed under a Creative Commons Attribution-NonCommercial 3.0 Unported Licence.

3.4 Carbon dioxide incorporation

3.4.1 Cubic $SrFeO_{3-\delta}$. Prior work has shown that carbonate (and other oxyanions) can be incorporated into many perovskite systems at temperatures below 1000 °C.[10] This has significant implications for the design of SOFC component materials. It is also predicted that in the synthesis of some perovskites such as $SrFeO_3$, some amount of carbonate will inevitably be incorporated. There is also a growing trend in research to synthesise materials at lower and lower temperatures such as sol–gel methods, where carbonate can be thermally stable within structures and its incorporation should not be omitted on grounds that it will be lost on heating.

The reaction which is proposed to take place in carbon dioxide incorporation mechanisms is $CO_2 + O^{2-} \rightarrow CO_3^{2-}$, which has an associated energy (analogous to the proton transfer term in the water incorporation mechanisms) of

Table 8 Lowest energy carbon dioxide incorporation energies for a 4 × 4 × 4 cubic $SrFeO_{2.7}$ supercell

Defect site	Incorporation mechanism	Formation energy/defect (eV)
FeO_6	$Fe_{Fe}^{\times} + CO_2^{(g)} + 7O_O^{\times} \rightarrow \left[(CO_3)_{Fe}^{'''''} + 4V_O^{\bullet\bullet}\right] + \frac{3}{2}O_i^{''} + \frac{1}{2}Fe_2O_3$	−1.97
FeO_5	$Fe_{Fe}^{\times} + CO_2^{(g)} + 4O_O^{\times} \rightarrow \left[(CO_3)_{Fe}^{'''''} + V_O^{\bullet\bullet}\right] + \frac{3}{2}V_O + \frac{1}{2}Fe_2O_3$	−2.18
	$Fe_{Fe}^{\times} + CO_2^{(g)} + 5O_O^{\times} \rightarrow \left[(CO_3)_{Fe}^{'''''} + 2V_O^{\bullet\bullet}\right] + \frac{1}{2}V_O^{\bullet\bullet} + \frac{1}{2}Fe_2O_3$	−2.20
FeO_4	$Fe_{Fe}^{\times} + CO_2^{(g)} + 4O_O^{\times} \rightarrow \left[(CO_3)_{Fe}^{'''''} + V_O^{\bullet\bullet}\right] + \frac{3}{2}V_O^{\bullet\bullet} + \frac{1}{2}Fe_2O_3$	−3.27
	$Fe_{Fe}^{\times} + CO_2^{(g)} + 5O_O^{\times} \rightarrow \left[(CO_3)_{Fe}^{'''''} + 2V_O^{\bullet\bullet}\right] + \frac{1}{2}V_O^{\bullet\bullet} + \frac{1}{2}Fe_2O_3$	−3.31
Oxygen	$CO_2(g) + O_O^{\times} \rightarrow (CO_3)_O^{\times}$	−2.58

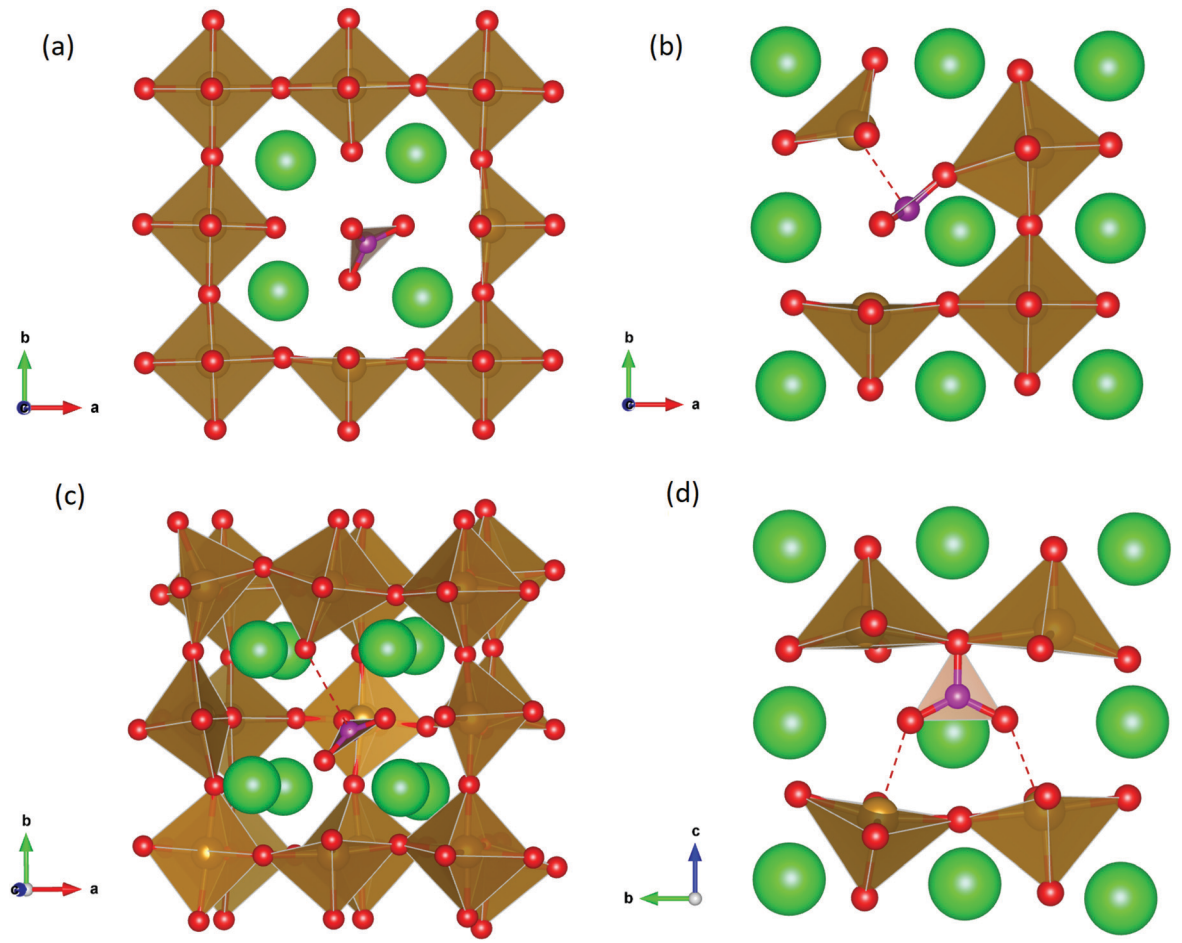

Fig. 6 Lowest-energy supercell carbonate defect optimised structures. In (a) and (b), carbonate defects on an iron site and on an oxygen site respectively are shown for pure cubic $SrFeO_3$. (c) and (d) show the same for the cubic $SrFeO_{2.7}$ supercell system.

Open Access Article. Published on 14 October 2020. Downloaded on 1/11/2026 11:58:37 AM.
This article is licensed under a Creative Commons Attribution-NonCommercial 3.0 Unported Licence.

Table 9 Carbon dioxide incorporation energies for a 1 × 3 × 3 brownmillerite $SrFeO_{2.5}$ supercell

Defect site	Incorporation mechanism	Formation energy/defect (eV)
FeO_6	$Fe_{Fe}^{\times} + CO_2^{(g)} + 5O_O^{\times} \rightarrow \left[(CO_3)_{Fe}^{'''''} + 2V_O^{\bullet\bullet}\right] + \frac{1}{2}V_O^{\bullet\bullet} + \frac{1}{2}Fe_2O_3$	0.65
	$Fe_{Fe}^{\times} + CO_2^{(g)} + 6O_O^{\times} \rightarrow \left[(CO_3)_{Fe}^{'''''} + 3V_O^{\bullet\bullet}\right] + \frac{1}{2}O_i^{''} + \frac{1}{2}Fe_2O_3$	0.09
FeO_4	$Fe_{Fe}^{\times} + CO_2^{(g)} + 6O_O^{\times} \rightarrow \left[(CO_3)_{Fe}^{'''''} + 3V_O\right] + \frac{1}{2}O_i^{''} + \frac{1}{2}Fe_2O_3$	−0.31
Both	$CO_2^{(g)} \rightarrow \frac{1}{2}\left[(CO_3)_{Fe}^{'''''} + 2V_O^{\bullet\bullet}\right] + \frac{1}{2}\left[(CO_3)_{Fe}^{'''''} + 3V_O\right] + \frac{1}{2}Fe_2O_3$	−0.12

−14.41 eV.[13] Possible identified carbon dioxide incorporation mechanisms are shown in Table 7 along with their respective incorporation energies.

Carbonate incorporation simulations were performed using the super cell method with a 6 × 6 × 6 unit cell size. The mechanisms and corresponding incorporation energies for carbonate in pure cubic $SrFeO_3$ are unfavourable as can be seen from results in Table 7. Our simulations suggest that it is unlikely that any carbonate incorporation mechanisms will occur naturally in cubic strontium ferrite unless it contains iron vacancies and surrounding oxygen vacancies as shown in Table 8. If one assumes existing vacancies however, the carbonate incorporation becomes favourable and the carbonate group is positioned on the iron site and parallel to the plane formed by the oxygen vacancies, as displayed in Fig. 6.

3.4.2 Brownmillerite $SrFeO_{2.5}$. The reasons for looking at carbon dioxide incorporation in $SrFeO_{2.5}$ mirror those for the cubic system with consideration for fuel cell application. As in the cubic system, the synthesis of $SrFeO_{2.5}$ usually involves heat treatment of $SrCO_3$ and Fe_2O_3 and so *via* lower-temperature routes such as sol–gel carbonate could be incorporated as a defect. Also, brownmillerite $SrFeO_{2.5}$ has recently been looked at for application in high-temperature sensors for O_2, CO_2 and CO.[34]

Relative to the cubic system, brownmillerite $SrFeO_{2.5}$ is less dense, making it intuitively more reasonable to allow a large carbonate anion to be accommodated in the structure, especially considering previous successful oxyanion doping into brownmillerite-type $Ba_2In_2O_5$.[5] It was expected that, similarly to the cubic case, carbonate would exist on the iron site and

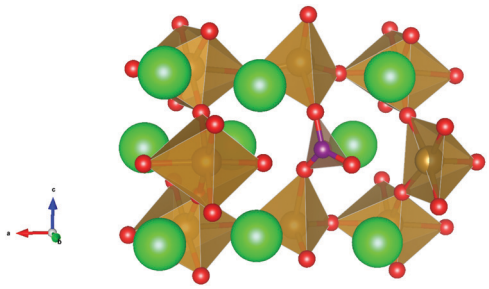

Fig. 7 Carbonate defect in brownmillerite $SrFeO_{2.5}$, involving a carbonate molecule on a tetrahedral iron site due to a carbon dioxide molecule reacting with the brownmillerite structure with an iron vacancy and two oxygen vacancies as described in mechanism 1a. Sr, Fe, O and C atoms are represented as green, brown, red and purple spheres respectively and Fe–O polyhedra and CO_3^{2-} units are represented in brown and purple respectively.

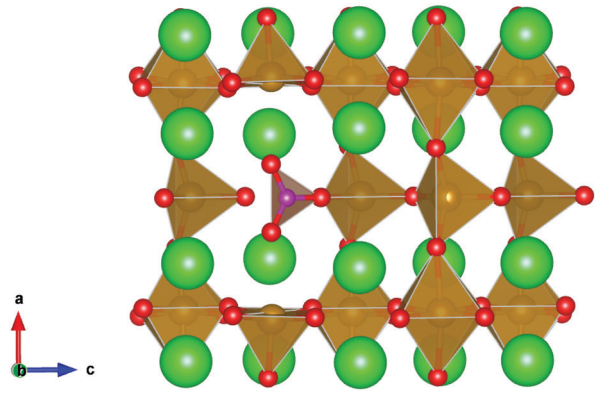

Fig. 8 Carbonate defect in brownmillerite $SrFeO_{2.5}$, involving a carbonate molecule on a tetrahedral iron site. Sr, Fe, O and C atoms are represented as green, brown, red and purple spheres respectively and Fe–O polyhedra and CO_3^{2-} units are represented in brown and purple respectively.

therefore require iron vacancies and a number of surrounding oxygen vacancies in the pure $SrFeO_{2.5}$ structure to accommodate it due to the similarity in structure and composition to the cubic system, and the large size of the carbonate anion.

The mechanisms are displayed in Table 9. Supercells consisting of 36 unit cells of brownmillerite $SrFeO_{2.5}$ have been used. Both carbonate incorporation during and after formation of strontium ferrite show favourable energies.

From Table 9 the coordination of the iron site on which the carbonate is placed shows a slight difference. The most favourable is when the carbonate is on the tetrahedral Fe site, which is perhaps not unexpected as this site is most likely to accommodate a trigonal planar carbonate ion, without too much disruption to the structure. The lowest energy arrangements for each are displayed are shown in Fig. 7 and 8.

4 Conclusions

In conclusion, this computational study shows that intrinsic Frenkel or Schottky defects in both pure cubic and brownmillerite-type $SrFeO_{3-\delta}$ systems are unlikely to form spontaneously. For pure cubic $SrFeO_3$, water incorporation is likely through $OH_O^{\bullet}$ defects in the cubic system with oxygen vacancies present and is also plausible in the brownmillerite system *via* mechanisms including both $OH_O^{\bullet}$ and $OH_i^{'}$ defects, the latter of which could significantly impact the oxide ion conductivity by increasing disorder.

Open Access Article. Published on 14 October 2020. Downloaded on 1/11/2026 11:58:37 AM.
This article is licensed under a Creative Commons Attribution-NonCommercial 3.0 Unported Licence.

Calculations in this work also show that carbon dioxide incorporation is unlikely in pure stoichiometric $SrFeO_3$, but if there are iron and oxygen vacancies, carbonate will be accommodated into the cubic structure on the iron site, despite CO_3^{2-} itself being an anion. Carbonate is known to behave similarly in the related Ruddlesden–Popper phase, $Sr_3Fe_{3-x}(CO_3)_xO_{6-O_{10-4x-y}}$[35] and the layered iron oxycarbonate $Sr_4Fe_2O_6(CO_3)$.[26] Sulphate and borate ions have also recently been doped into $SrFeO_{3-\delta}$.[3] The implications for SOFC application are that the structural differences between pure and defective structures will inevitably affect the conductivity and function and should therefore be considered in future studies. In addition, given that there is a growing propensity for utilizing lower temperature (sol–gel) routes to synthesise such fuel cell materials, the results present here imply that the potential incorporation of carbonate and water needs to be considered for these materials.

Conflicts of interest

There are no conflicts to declare.

Acknowledgements

The authors would like to thank the EPSRC-funded CDT for Fuel Cells and their Fuels (EP/L015749/1) for funding LJF's studentship. PRS would like to thank the Leverhulme Trust (Exploring carbonate incorporation in ''oxide'' materials: the hidden dopant in Materials Chemistry (RPG-2017-011)) and the EPSRC for funding the JUICED Hub (Joint University Industry Consortium for Energy (Materials) and Devices Hub EP/R023662/1).

References

1 N. Mahato, A. Banerjee, A. Gupta, S. Omar and K. Balani, *Prog. Mater. Sci.*, 2015, **72**, 141–337.
2 A. Jun, J. Kim, J. Shin and G. Kim, *ChemElectroChem*, 2016, **3**, 511–530.
3 A. Jarvis and P. R. Slater, *Crystals*, 2017, **7**, 169.
4 J. M. Porras-Vazquez, T. Pike, C. A. Hancock, J. F. Marco, F. J. Berry and P. R. Slater, *J. Mater. Chem. A*, 2013, **1**, 11834–11841.
5 J. F. Shin, A. Orera, D. Apperley and P. Slater, *J. Mater. Chem.*, 2011, **21**, 874–879.
6 N. Lu, Y. Wang, S. Qiao, H.-B. Li, Q. He, Z. Li, M. Wang, J. Zhang, S. C. Tsang and J. Guo, *et al.*, 2018, arXiv preprint, arXiv:1811.10802.
7 P. Gallagher, *J. Chem. Phys.*, 1964, **41**, 2429.
8 Y. Teraoka, S. Furukawa, H. Zhang and N. Yamazoe, *Nippon Kagaku Kaishi*, 1988, 1084–1089.
9 T. Das, J. D. Nicholas and Y. Qi, *J. Mater. Chem. A*, 2017, **5**, 4493–4506.
10 C. Hancock, J. Porras-Vazquez, P. Keenan and P. Slater, *Dalton Trans.*, 2015, **44**, 10559–10569.
11 O. Merkulov, E. Naumovich, M. Patrakeev, A. Markov, E. Shalaeva, V. Kharton, E. Tsipis, J. Waerenborgh, I. Leonidov and V. Kozhevnikov, *J. Solid State Electrochem.*, 2018, **22**, 727–737.
12 A. J. McSloy, P. F. Kelly, P. R. Slater and P. M. Panchmatia, *Phys. Chem. Chem. Phys.*, 2016, **18**, 26284–26290.
13 A. J. McSloy, I. Trussov, A. Jarvis, D. J. Cooke, P. R. Slater and P. M. Panchmatia, *J. Phys. Chem. C*, 2018, **122**, 1061–1069.
14 J. D. Gale, *J. Chem. Soc., Faraday Trans.*, 1997, **93**, 629–637.
15 J. Gulp and A. Rohl, *Mol. Simul.*, 2003, **29**, 291–341.
16 K. Momma and F. Izumi, *J. Appl. Crystallogr.*, 2008, **41**, 653–658.
17 R. A. Buckingham, *Proc. R. Soc. London, Ser. A*, 1938, **168**, 264–283.
18 B. Dick Jr and A. Overhauser, *Phys. Rev.*, 1958, **112**, 90.
19 G. Lewis and C. Catlow, *J. Phys. C: Solid State Phys.*, 1985, **18**, 1149.
20 M. Cherry, M. S. Islam and C. Catlow, *J. Solid State Chem.*, 1995, **118**, 125–132.
21 G. C. Mather, M. S. Islam and F. M. Figueiredo, *Adv. Funct. Mater.*, 2007, **17**, 905–912.
22 P. M. Morse, *Phys. Rev.*, 1929, **34**, 57.
23 P. M. Panchmatia, A. Orera, E. Kendrick, J. V. Hanna, M. E. Smith, P. Slater and M. Islam, *J. Mater. Chem.*, 2010, **20**, 2766–2772.
24 S. Kerisit and S. C. Parker, *J. Am. Chem. Soc.*, 2004, **126**, 10152–10161.
25 T. Archer, S. Birse, M. T. Dove, S. Redfern, J. D. Gale and R. Cygan, *Phys. Chem. Miner.*, 2003, **30**, 416–424.
26 K. Yamaura, Q. Huang, J. Lynn, R. Erwin and R. J. Cava, *J. Solid State Chem.*, 2000, **152**, 374–380.
27 N. Nevskij, B. Ivanov-Ehmin, N. Nevskaya, G. Z. Kaziev and N. V. Belov, *Dokl. Akad. Nauk SSSR*, 1982, **264**, 857–858.
28 N. Mott and M. Littleton, *Trans. Faraday Soc.*, 1938, **34**, 485–499.
29 J. Hodges, S. Short, J. Jorgensen, X. Xiong, B. Dabrowski, S. Mini and C. Kimball, *J. Solid State Chem.*, 2000, **151**, 190–209.
30 M. Harder and H. Müller-Buschbaum, *Z. Anorg. Allg. Chem.*, 1980, **464**, 169–175.
31 C. A. Fisher and M. S. Islam, *J. Mater. Chem.*, 2005, **15**, 3200–3207.
32 K. Wright, R. Freer and C. Catlow, *Phys. Chem. Miner.*, 1994, **20**, 500–503.
33 Y. Takeda, K. Kanno, T. Takada, O. Yamamoto, M. Takano, N. Nakayama and Y. Bando, *J. Solid State Chem.*, 1986, **63**, 237–249.
34 S. B. Karki, R. K. Hona and F. Ramezanipour, *J. Electron. Mater.*, 2020, **49**, 1557–1567.
35 Y. Bréard, C. Michel, M. Hervieu and B. Raveau, *J. Mater. Chem.*, 2000, **10**, 1043–1045.